RSC Applied Interfaces

ROYAL SOCIETY OF CHEMISTRY

PAPER

View Article Online
View Journal

Cite this: DOI: 10.1039/d5lf00374a

Open-air plasma treatment of polypropylene fabrics for enhanced metal oxide nanoparticle adhesion: the effect of oxide acid–base character

Owen C. Grimm, Saurabh Karande and James E. Whitten *

Methods to attach metal oxide nanoparticles (MONPs) to inert supports such as polymers, fabrics and membranes, are important for applications that include filtration, lithium-ion battery separators, and photocatalysis. In the present study, a high-throughput method that consists of open-air plasma treatment of polypropylene (PP) knitted fabric, followed by spray-coating with ethanolic colloidal suspensions of various MONPs, has been investigated. X-ray photoelectron spectroscopy (XPS) indicates that open-air plasma treatment forms surface hydroxyl, carbonyl and carboxylic acid groups. The water contact angle of similarly treated spin-coated PP films decreases to 80°, compared to 97° for untreated PP. XPS and field emission scanning electron microscopy (FE-SEM) of plasma-treated and untreated controls spray-coated with MONPs, rinsed, and ultrasonicated in ethanol show that plasma treatment leads to enhanced particle adhesion. MONPs that act as weak Lewis acids, such as ZnO, MgO and In_2O_3, essentially completely coat the fibers, while more acidic MONPS, such as CeO_2, SiO_x, SnO_2, TiO_2, and WO_3, adhere relatively poorly, even on plasma-treated fabric. Metal oxide coverage, determined by XPS, inversely correlates with the polarizing power of the cation in the metal oxide. It is hypothesized that the metal oxide hydroxyl groups play a key role in adhesion, with strong Lewis acid MONPs exhibiting weaker hydrogen bonding to the polar functional groups (*e.g.*, carbonyl groups) of the plasma-treated PP. Photocatalytic application of this method of attaching nanoparticles is demonstrated by ultraviolet light-induced decomposition of methyl paraoxon by ZnO-functionalized PP.

Received 27th November 2025,
Accepted 14th April 2026

DOI: 10.1039/d5lf00374a

rsc.li/RSCApplInter

Introduction

In several emerging technologies, it is important to attach nanoparticles to fibers, fabrics or membranes. Applications of supported metal oxide nanoparticles (MONPs) or metal–organic frameworks (MOFs) include gas, aerosol or liquid filtration,[1–3] photocatalysis,[4–11] and separator membranes for lithium-ion batteries.[12,13] In photocatalysis, for example, it is desirable to support MONPs in such a way that they present a large surface area to the solution or gas in which they are immersed, and this has been achieved using natural and synthetic fibers, and even high surface area 3-D printed polymers.[4–11]

Polypropylene (PP) is one of the most processible polymers because of its relatively low melting point and ease of extrusion. Methods that have been used to attach MONPs and MOFs to PP fibers and fabrics include gamma radiation-induced grafting,[14] spin-coating,[15] atomic layer deposition (ALD),[16–20] and plasma treatment.[21,22] Toward the goal of industrialization of ALD with spatial control, Gurbandurdyyev *et al.*[19] demonstrated atmospheric pressure ALD of ZnO on spun-bond PP and cotton fabrics. Vacuum plasma was used by de Rancourt *et al.*[21] to activate PP and graft polymer-encapsulated ZnO onto the PP. Interestingly, the authors noted that non-functionalized ZnO was also observed to adhere to the plasma-treated PP.

Our group demonstrated that PP knitted fabrics exposed to conventional plasma, immersed in colloidal ethanolic suspensions of ZnO or TiO_2 nanoparticles, and then rinsed and ultrasonicated in pure ethanol exhibited enhanced NP adhesion.[22] In that study, it was observed that ZnO NPs adhered with higher surface density than TiO_2 NPs, and it was postulated that the difference was due to the somewhat smaller size of the ZnO (20–40 nm) compared to the TiO_2 (30–50 nm). As we will show, however, this is no longer believed to be the main factor.

Commercially, open-air plasma treatment has been used to increase the adhesion of glues, dyes and inks to polymers,[23] to modify the surface properties of styrene–butadiene–styrene rubber,[24] to prepare surfaces for biomaterial applications,[23,25] and to stabilize the oxide on semiconductors for electronic applications.[26] In the present study, we have attempted to

Department of Chemistry, University of Massachusetts Lowell, Lowell, MA 01854, USA. E-mail: James_Whitten@uml.edu; Fax: (978) 934 3013; Tel: (978) 934 3666

develop a high-throughput method, using open-air plasma treatment instead of vacuum plasma, to functionalize PP with MONPs. Furthermore, activated PP fabrics have been spray-coated with, instead of immersed in, colloidal MONP suspensions.

To the best of our knowledge, the relative reactivity of various MONPs with plasma-treated surfaces has not been investigated. This reactivity may affect the strength of adhesion and is expected to depend on properties of the MONPs such as hydroxyl surface density, the presence of surface defects, and the acid–base character of the oxide. The latter property is most conveniently described within the Lewis and Brønsted definition of acidity and basicity.[27,28] In this regard, a metal oxide may be considered a Lewis acid if exposed, coordinatively unsaturated cations can accept an electron pair to form a dative or coordination bond. It may be considered a base if it possesses a nonbonding electron pair that can be donated to form a bond.

In this work, the effect of open-air plasma treatment on the surface chemistry of PP has been investigated with X-ray photoelectron spectroscopy (XPS). The adhesion of seven MONPs, with similar particles size, to plasma-treated knitted PP fabric has been assessed using XPS and field-emission electron microscopy (FE-SEM). It is shown that the various MONPs do not adhere equally to plasma-treated PP, with the acid–base character of the MONP dictating success of the method. This work is important toward the goal of developing high-throughput methods of functionalizing materials, including polymeric fibers, for a variety of applications. The use of this method for photocatalysis is demonstrated using a ZnO-functionalized PP fabric.

Experimental section

Polypropylene films and fabrics

Two types of PP samples were prepared. Spin-coated PP films on *ca.* 10 × 10 × 1 mm silicon wafers were prepared from low molecular weight PP (M_w = 12 kDa) purchased from Aldrich Chemical Company (stock no. 428116) using the following procedure. Approximately 0.50 g of PP powder was placed in a glass scintillation vial, and 5.0 g of *o*-xylene and a small magnetic stir bar were added to the vial. The outside of the vial was wrapped in two layers of aluminum foil and placed on a stir/hot plate. The vial was then heated to *ca.* 130–135 °C but kept below the boiling point of *o*-xylene (144 °C) until the PP dissolved. A silicon wafer was placed on the spin-coater chuck that was similar to, or smaller in diameter than, the silicon wafer; both were heated with a heat gun, and *ca.* 100 μL of hot PP/*o*-xylene was pipetted onto the hot, spinning silicon wafer. A spin-coating speed of 2500 rpm for 30 s. was employed. To realize uniform films, it is imperative that the silicon wafer is hot and that the entire process is carried out quickly so that the PP does not settle out of solution.

The second type of PP sample consisted of knitted PP fabric prepared from PP fiber, with a Tex number of 47, purchased from Goodfellow, Inc (stock no. PP305747/1). The fiber consisted of 86 filaments, each with diameter of 0.028 mm. The fiber (with an estimated diameter of *ca.* 0.2 mm) was knitted into a "sock" material. Prior to use, the knitted PP fabric was ultrasonicated in a *ca.* 0.5 wt% aqueous Triton-X solution for 30 min. It was then ultrasonicated between 7 and 10 times for a 30 min duration, each using a new batch of distilled water, until absolutely no suds could be seen by the naked eye, to remove any residual surfactant.

Plasma treatment and spray-coating

To prepare the MONP-coated PP fabrics, absolute ethanol (Fisher Scientific) was used, and the MONPs were either from Nanoparticles and Amorphous Materials, Inc. or MTI, Inc. The primary particle sizes were all in the range of 10–70 nm, with more details provided in Table 1. Fig. 1 depicts the process used to activate the PP fabric, spray-coat it with MONPs and remove loosely bound particles. Fabric samples were plasma treated using an open-air plasma system (model FG5001) from PlasmaTreat, Inc., with "breathing air" as the gas source; other gases cannot be used with this instrument. The distance between the nozzle (part no. 22890) and fabric was set to 5/8 in., and the PP fabric was treated in one of two ways. Either the nozzle was kept stationary, and the fabric was attached to a movable conveyor belt, or the fabric was kept stationary, and the nozzle motion was controlled by a Cartesian robot. Either way, the linear speed was *ca.* 6.0 cm s^{-1}, and the area treatment rate was *ca.* 30 cm^2 s^{-1}. The nozzle was passed over the fabric 3 times, unless otherwise stated, and both sides of the fabric were treated. After plasma treatment, both sides of the PP were spray-coated, using an air brush, with a *ca.* 5 wt% ethanolic MONP suspension. This had been prepared by ultrasonicating the suspension using a Branson 2510 ultrasonicator (42 kHz, 100 W), and the dispersion was spray-coated immediately before it settled. After allowing the swatch briefly to dry in air, it was ultrasonicated in absolute ethanol. Typically, sonication in clean ethanol was performed three times, for 5 min each. The ultrasonicated PP swatch was air-dried overnight prior to further evaluation. In most cases, a control sample went through the same process except that it was not plasma-treated.

Characterization

The water contact angles (WCA) of the PP films on silicon wafers were measured using an Ossila sessile drop contact angle goniometer with a drop volume of 10 μL of distilled water. Error bars were estimated from repeated measurements on the same sample. Attenuated total reflectance (ATR) was measured with a Nicolet iS50 Fourier transform infrared spectrometer by placing a doubled-over piece of PP fabric between the piston and the sapphire window of the ATR accessory. The background was acquired with no sample in the ATR accessory, and a total of 416 scans were averaged with a resolution of 0.5 cm^{-1}. For some samples, thermal gravimetric analysis (TGA) was used to attempt to quantify the mass of MONP on the PP swatch. For these measurements, the samples were heated in nitrogen up to 800 °C at a heating rate of 20 °C min^{-1}. For pure PP, the mass

Table 1 MONP properties and XPS metal-to-carbon atomic ratios for functionalized PP fabrics

Metal oxide	Vendor[a]	Vendor part no.	Nominal particle Size[b] (nm)	Metal/C atomic ratio (Std Dev)[c]	Mass % of MONP in PP swatch (Std Dev)[d]	Polarizing power of the metal oxide cation
CeO_2	NanoAmor	1406RE	15–30	0.072 (0.025)	—	4.1
In_2O_3	NanoAmor	2710TN	30–50	0.20	1.4	3.9
MgO	NanoAmor	3315HT	20	0.67 (0.09)	2.4	2.8
SiO_x	NanoAmor	4860MR	28	0.10	—	15.4
SnO_2	NanoAmor	5010FY	61	0.067	—	5.8
TiO_2 (anatase)	NanoAmor	5240HT	10–30	0.056 (0.017)	—	6.6
WO_3	MTI, Inc.	NPWO3	30–70	0	—	10.2
ZnO	NanoAmor	5811HT	30	0.50 (0.23)	2.9 (0.9)	3.4

[a] "NanoAmor" denotes Nanostructured and Amorphous Materials, Inc. [b] Refers to primary particle size from product specifications. [c] The standard deviation was calculated for samples in which more than one MONP-covered PP of the same particle was analyzed by XPS (from different batches). If no standard deviation is included, then only one sample was run. [d] Determined from TGA analysis of metal oxide-functionalized PP sample. Reliable data were only obtainable for the samples with a high metal oxide surface concentration. Multiple samples were measured for ZnO from completely different batches, yielding the standard deviation in parentheses.

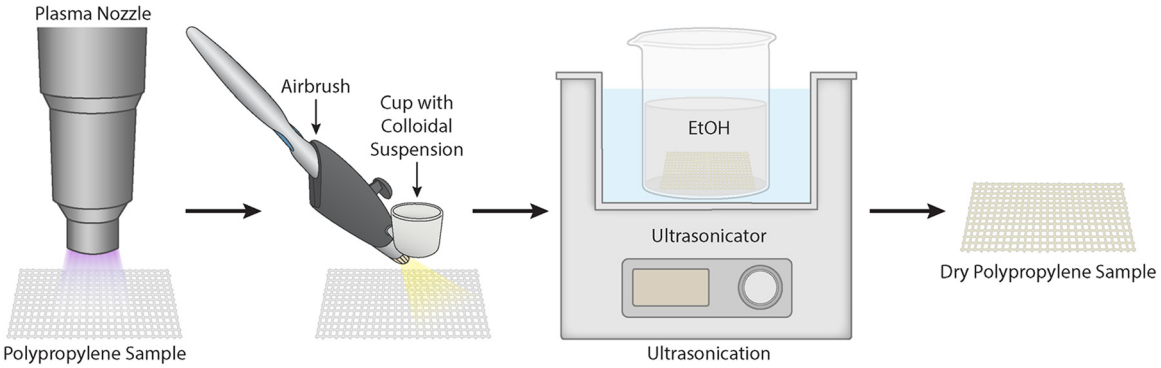

Fig. 1 Schematic of the steps for functionalizing PP knitted fabric with MONPs. The fabric is open-air plasma treated and then spray-coated with an ethanolic colloidal suspension of the MONP. The fabric is then rinsed with ethanol and ultrasonicated several times in clean ethanol.

decreased to essentially zero. For MONP-covered samples with significant amounts of MONP, there was a non-negligible residual mass remaining, and this was used to estimate the mass percentage contributed by the MONPs on the PP fabric.

Field-emission scanning electron microscopy (FE-SEM) was performed with a JEOL JSM 7401F microscope using beam energies in the range of 3–7 keV or a Zeiss Auriga 40 FIB-SEM with a beam energy of 5 keV. Samples were adhered to a sample stub with carbon tape and sputter-coated with a thin layer of gold prior to imaging.

XPS was performed using a ThermoFisher Sigma Probe instrument equipped with a non-monochromatized AlKα X-ray source ($h\nu$ = 1486.6 eV). The PP samples were folded over on themselves (to prevent analysis of any material under the voids in the PP knitted material) and adhered to a transferrable sample stage with vacuum compatible, adhesive copper tape. The stage was loaded into the preparation chamber for pump-down prior to transferring them to the analysis chamber, which had a vacuum of 10^{-8} Torr range during analysis. The kinetic energies of the ejected photoelectrons were measured in fixed analyzer transmission mode, with a pass energy of 20 eV and an energy step size of 0.05 eV. The binding energy scale is referenced to the spectroscopic Fermi level. In the case of PP fabric, no charge correction was needed, with the main C 1s component having a binding energy of *ca.* 285 eV, as expected.[29] For metal oxide containing samples, the spectra were shifted by the energy necessary to align the metal peaks of the oxides to their known values.[30] Background subtraction, peak fitting and quantitative analysis were performed using the Sigma Probe's Avantage software, with the areas of the peaks (after accounting for the transmission function of the instrument) divided by their Scofield sensitivity factors.

Photocatalysis measurements

Demonstration of the use of a ZnO-functionalized PP fabric for photocatalysis was performed by filling two 1 cm pathlength quartz cuvettes each with 3.0 ml of 8×10^{-5} M aqueous methyl paraoxon, also known as paraoxon-methyl (Sigma-Aldrich "PESTANAL" grade). **CAUTION**: methyl paraoxon is extremely toxic and potentially fatal to humans, even in small quantities. It must be handled with extreme caution and only by an expert at handling toxic chemicals. Furthermore, it must be discarded in an approved manner to avoid environmental hazards. Into each cuvette, a miniature Teflon-coated stir bar and 0.034 g piece of PP fabric was added. One of these PP fabrics was functionalized with ZnO, and one was an unfunctionalized

control. In both cases, the fabric pieces floated to the top of the cuvette because of their lower density. The cuvettes were stoppered and allowed to stir overnight in the dark. The next day, the cuvettes were equivalently irradiated by a 365 nm pen-ray lamp (AnalytikJena, no. 90-0019-01) while stirring their contents. The optical power of the light at the cuvettes was measured as 1.6 mW cm^{-2}. A Perkin Elmer Lambda 750, with 1 cm^{-1} resolution, was used for UV-vis absorbance measurements *versus* irradiation time. Because the PP fabrics were at the top of the cuvette, they did not interfere with the UV-vis measurements, and the cuvettes remained clear, with no evidence of particle loss from the fabrics.

Results and discussion

Open-air plasma treatment of PP substrates

As discussed earlier, plasma treatment of PP has been previously investigated.[21–23] However, few studies have reported the use of open-air (*i.e.*, atmospheric) plasma treatment of PP toward the goal of high-throughput processing. Because of differences between open-air and traditional (*i.e.*, vacuum) plasma treatment, it was necessary to measure its effects towards the goal of enhancing MONP adhesion. To optimize the plasma dose, silicon wafer samples that had been spin-coated with low molecular weight PP were placed on the conveyor belt and exposed to the plasma nozzle for different "numbers of passes", as defined earlier. Fig. 2 shows the WCA as a function of number of passes. The unexposed film exhibited a value of 97°. By three passes, the WCA decreased to 80°, and additional plasma treatment decreased it to *ca.* 76°. While the measured value for 5 passes (72°) is lower than that for more passes, it is within the error bar of the "final" value of *ca.* 76°. Because most of the decrease in WCA occurred after only a few passes, and to minimize polymer chain damage, three passes were chosen for subsequent experiments in this paper unless otherwise stated.

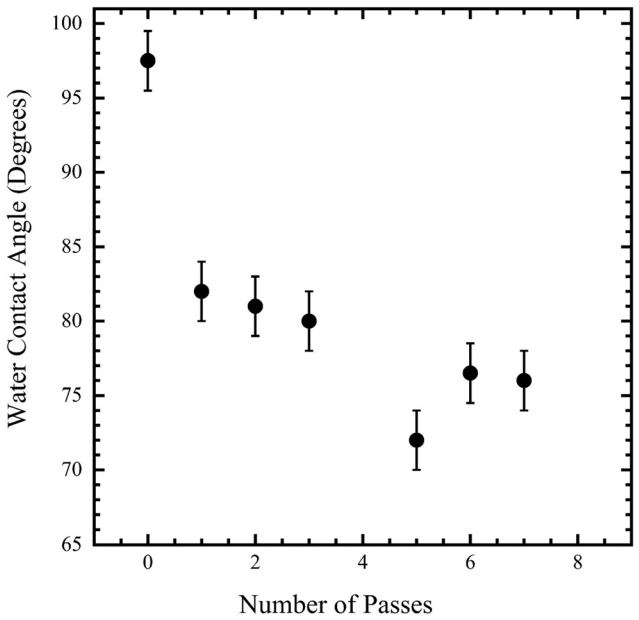

Fig. 2 Water contact angle (WCA) of open-air plasma treated PP spin-coated on glass *versus* the number of passes under the plasma nozzle.

Fig. 3 shows XPS spectra of unexposed and plasma-exposed PP swatches. The unexposed sample exhibits a C 1s spectrum with only one component at 285.0 eV, due to aliphatic carbon atoms in the PP chain. However, a small amount of oxygen is present at 533.6 eV, possibly due to oxidation during extrusion of the PP fibers. The O/C atomic ratio is 0.086. Plasma treatment causes emergence of higher binding energy component at 287.0 eV, due to formation of surface carbonyl/carboxylate groups. The oxidized-to-aliphatic carbon area ratio in the plasma-treated sample is 0.13. Plasma treatment causes the O/C atomic ratio to increase to 0.19 and the O 1s peak to shift to 532.2 eV. XPS of plasma-treated PP surfaces has previously been reported,[21,31,32] and our results are in general agreement with those, with high binding energy C 1s components in the range of 287 to 290 eV being detected due to plasma treatment.

A portion of the ATR spectra of untreated and plasma-treated PP fabrics is displayed in Fig. 4. The strong peaks at 1376 and 1450 cm^{-1} are due to CH_3 and CH_2 deformations, respectively.[33,34] The peak at 1735 cm^{-1} is due to carbonyl groups,[33] probably ketone or aldehyde groups, which are present in both samples. This is consistent with the XPS results, which showed oxygen present even in the untreated sample. Oxygen present in untreated PP is likely due to a small amount of oxidation that occurs during polymer extrusion, which occurs at an elevated temperature. Plasma treatment causes the oxygen-related peak to increase in intensity and a new feature to emerge at 1626 cm^{-1}; we assign this to enolized β-diketone groups.[33] This indicates that as more ketone groups are formed from plasma treatment, the probability of two being separated from each other by a single carbon atom in the chain becomes significant. While this peak is very weak, it should be realized that (unlike XPS), ATR is not a surface-sensitive technique. However, it offers the advantage of higher energy resolution and molecular structure sensitivity compared to XPS. Relatively high concentrations of high cross-section IR-active species in the near-surface region may often be detected in ATR, even if only as small peaks. The small features at 1540 and 1575 cm^{-1} in the spectrum of the untreated fabric are likely due to carboxylate groups involved in coordinating to contaminating metal ions[35] that are removed by plasma treatment. Because plasma treatment generally affects only a small depth of a nonporous surface, the observation of the 1626 peak and increased 1735 cm^{-1} peak intensity in ATR indicates that the carbonyl groups are present with a relatively high concentration in the near-surface region.

Deposition of MONPs on open-air plasma-treated PP

Initial experiments to assess nanoparticle adhesion to plasma-treated PP were performed using ZnO NPs because of their high

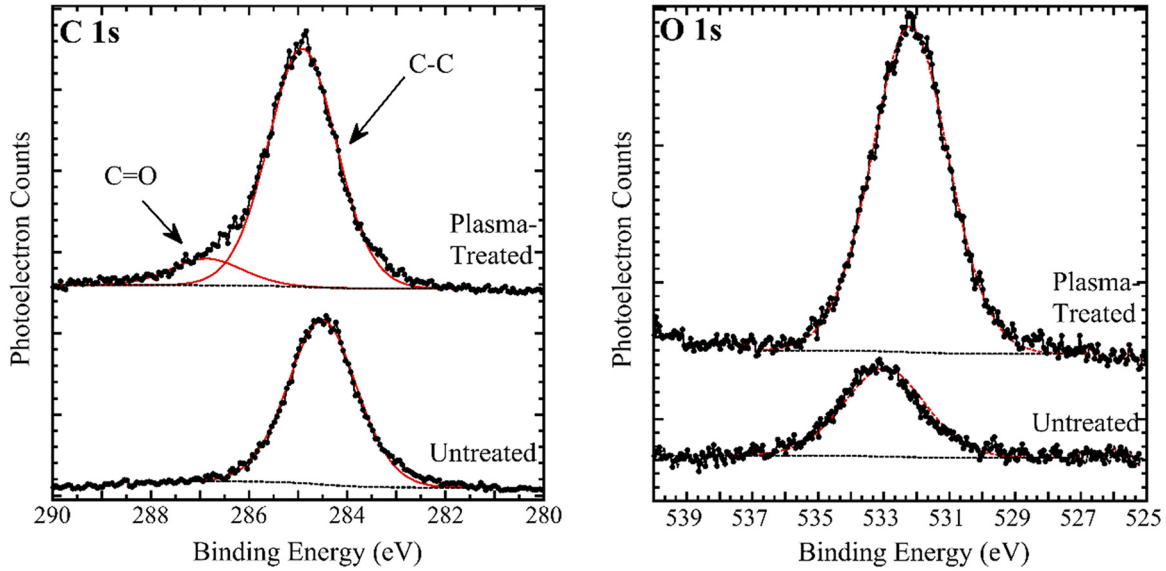

Fig. 3 AlKα charge-corrected XPS of the C 1s and O 1s regions of untreated and plasma-treated PP (3 passes). The solid data points are the raw XPS data, and the red curves are peak fits.

reactivity with respect to gas adsorption[36,37] and photocatalysis applications.[5,8,38,39] Fig. 5 includes FE-SEM images of PP samples, with and without plasma treatment, that were subsequently spray-coated with ZnO NPs, ultrasonicated in ethanol and then air-dried. The plasma-treated sample contains a dramatically greater ZnO surface concentration compared to the untreated sample. XPS is complementary to SEM in that it interrogates a larger region of the sample. Zn 2p spectra are included in Fig. 5 and substantiate plasma-induced adhesion, with the Zn 2p signal being significantly higher for the plasma-treated sample. The Zn/C atomic ratios for the untreated and plasma-treated samples are 0.044 and 0.38, respectively. Table 1 includes the average XPS Zn/C atomic ratio of 0.50 ± 0.23 for several PP samples that were spray-coated with ZnO NPs and ultrasonicated.

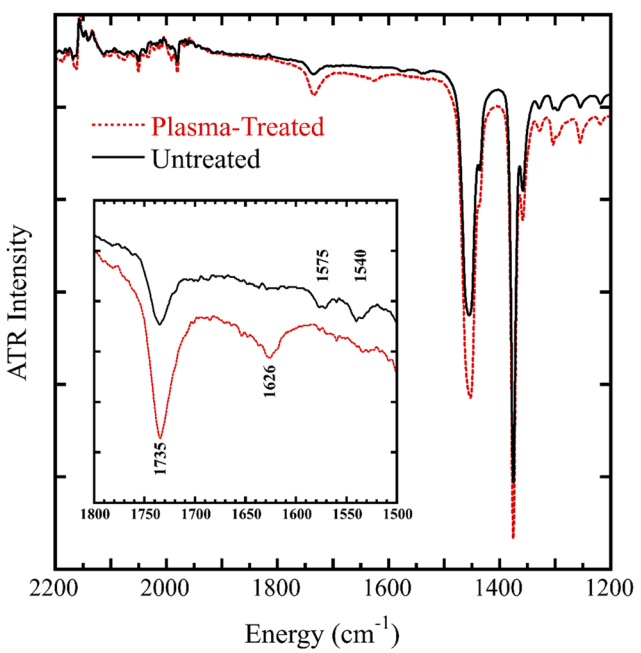

Fig. 4 A portion of the ATR spectrum of untreated and plasma-treated PP fabric (3 passes). The inset shows expansion of the ketone region of the spectrum. Some oxidation is present in the untreated fabric, as discussed in the text. However, plasma treatment enhances the 1735 cm^{-1} peak and causes emergence of a peak at 1626 cm^{-1}.

Analogous results were obtained for MgO NPs, as shown in Fig. 6. Similar to ZnO, significantly higher surface concentration is observed in the SEM of plasma-treated PP compared to untreated PP, and Mg 2p XPS confirms more MgO on the treated fabric. The Mg/C atomic ratios are 0.07 and 0.60 for the untreated and plasma-treated samples, respectively, for the particular samples shown in the figure. Table 1 includes the average value of 0.67 ± 0.09 from multiple samples.

This methodology was also explored for other MONPs, and FE-SEM images are displayed in Fig. 7 for TiO_2, CeO_2, SiO_x, SnO_2, In_2O_3 and WO_3 nanoparticles deposited on plasma-treated PP, rinsed with ethanol, ultrasonicated in ethanol and dried. Notably, the nanoparticles do not have equal affinity for the plasma-treated PP; indium oxide exhibits a significantly higher surface concentration than the others, and tungsten oxide shows the smallest. A summary of the XPS metal-to-carbon atomic ratios is included in Table 1 and in Fig. 8a.

The role of Lewis acid character in MONP adhesion

Data in the previous section indicate that MONP adhesion to plasma-treated PP follows the order: MgO > ZnO > In_2O_3 > CeO_2 = SnO_2 = SiO_x > TiO_2 > WO_3. To exclude the possibility that differing degrees of agglomeration of the MONPs during spray-coating may be responsible for the

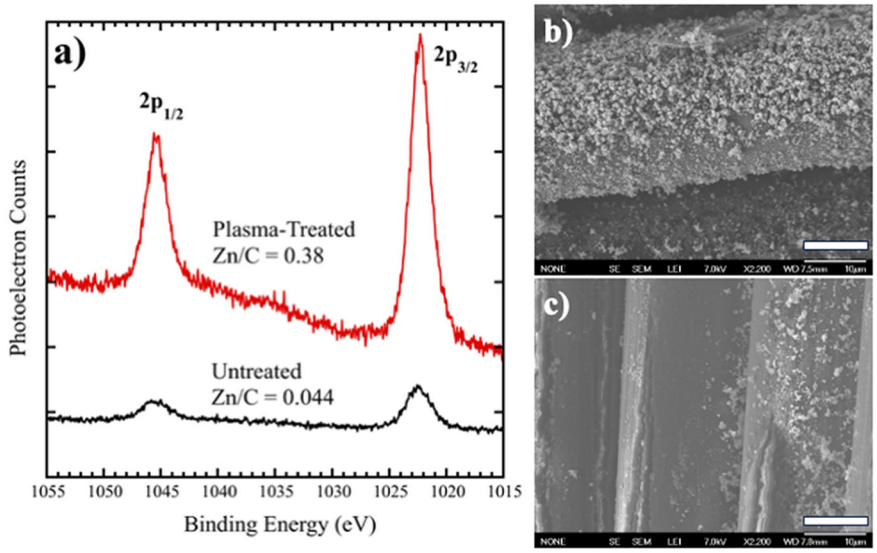

Fig. 5 (a) AlKα charge-corrected XPS of the Zn 2p region of untreated and plasma-treated PP fabrics (3 passes) that were functionalized with ZnO NPs; (b) FE-SEM image of ZnO NPs on plasma-treated fabric and (c) similar image for untreated PP fabric. The scale bars represent a length of 10 microns.

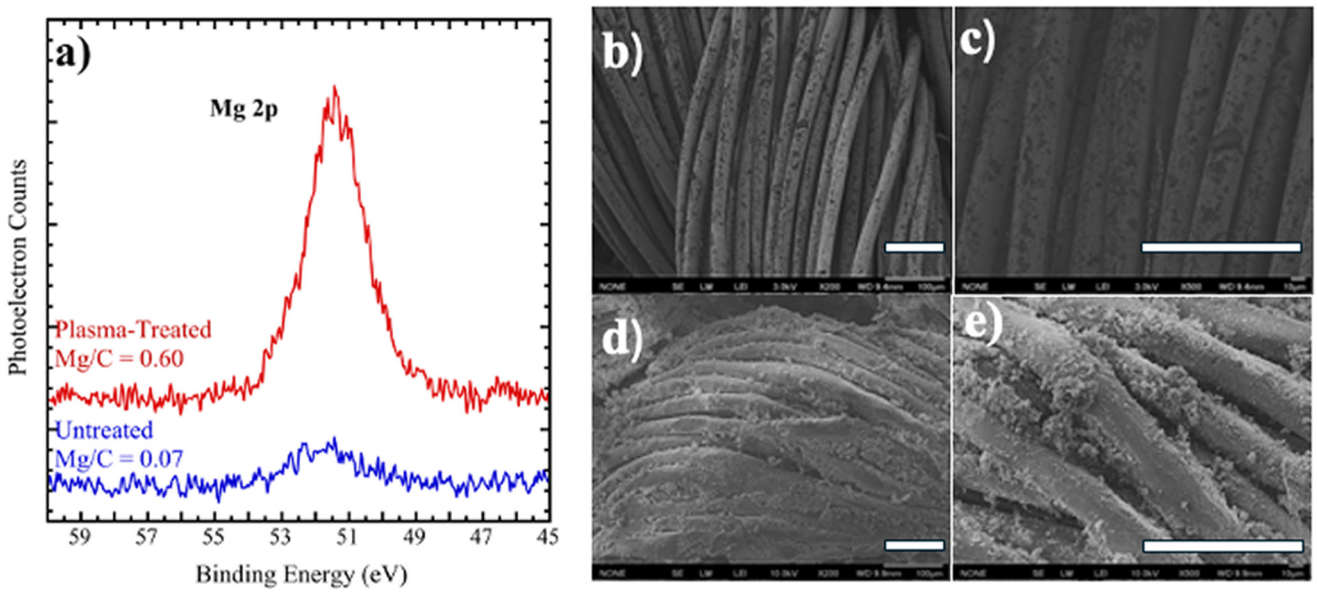

Fig. 6 (a) AlKα charge-corrected XPS of the Mg 2p region of untreated and plasma-treated PP fabrics (3 passes) that were functionalized with MgO NPs. (b and c) FE-SEM images of MgO NPs on plasma-treated PP fabric; (d and e) similar images of MgO NPs on untreated PP fabric. The scale bars represent a length of 100 microns.

observed order, FE-SEM images of several of the MONPs similarly spray-coated onto glass slides were acquired. Fig. 9 displays FE-SEM images of CeO_2, MgO, TiO_2, and ZnO. These were chosen because they vary dramatically in how well they adhere to the plasma-treated PP surface. The average agglomerated particle size is 249 ± 105 nm, 398 ± 202 nm, 347 ± 153 nm, and 369 ± 117 nm for CeO_2, MgO, TiO_2 and ZnO, respectively. If it were to play a role, smaller agglomerates would be expected to have more contact sites between the particles and the polymer surface and to lead to better adhesion. The similar agglomeration sizes and the fact that CeO_2, which has somewhat smaller agglomerates than the others but actually adheres poorly, strongly suggests that this is not a major factor in the observed order.

Magnesium oxide and zinc oxide are relatively weak Lewis acids, while tungsten oxide is a strong Lewis acid.[27] One way to quantify Lewis acidity is to calculate the polarizing power of the metal cation, which is defined as its charge-to-radius ratio. The assumption in correlating polarizing power with

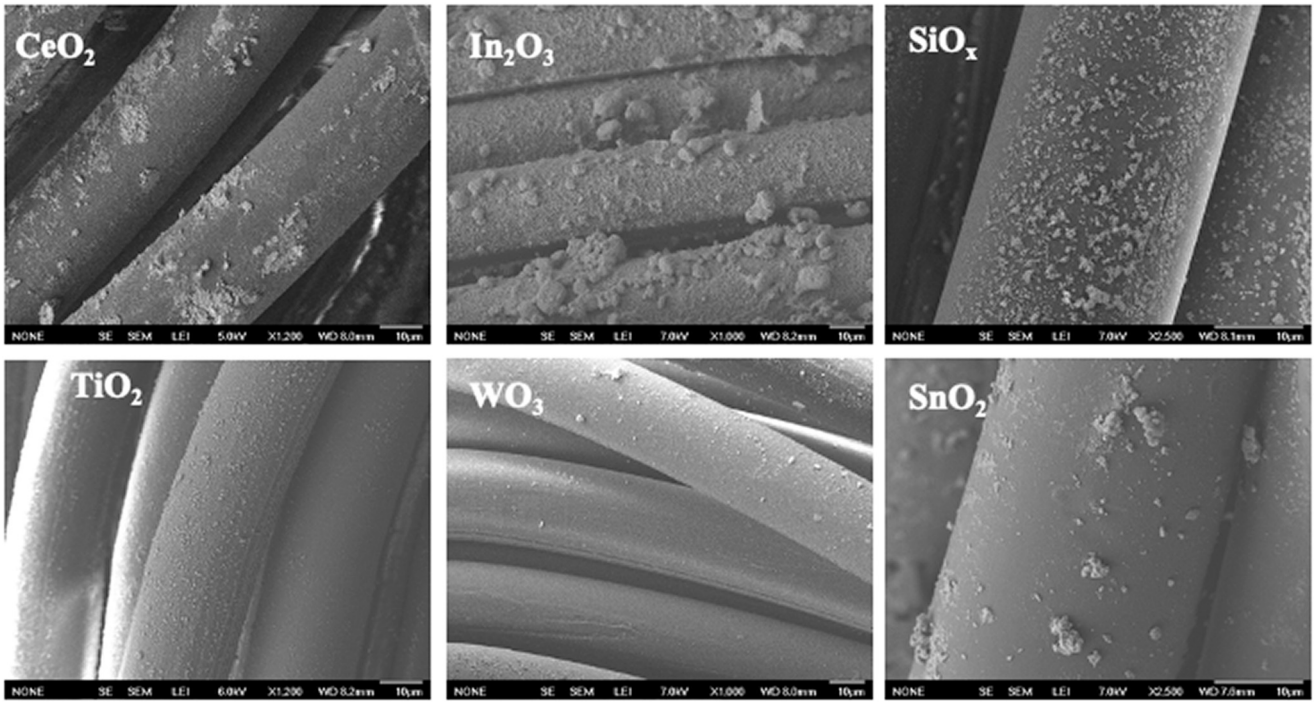

Fig. 7 FE-SEM images of ceria, indium oxide, silica, titania, tungsten oxide, and tin oxide NPs on plasma-treated PP (3 passes), with the identity of the MONP included in the image.

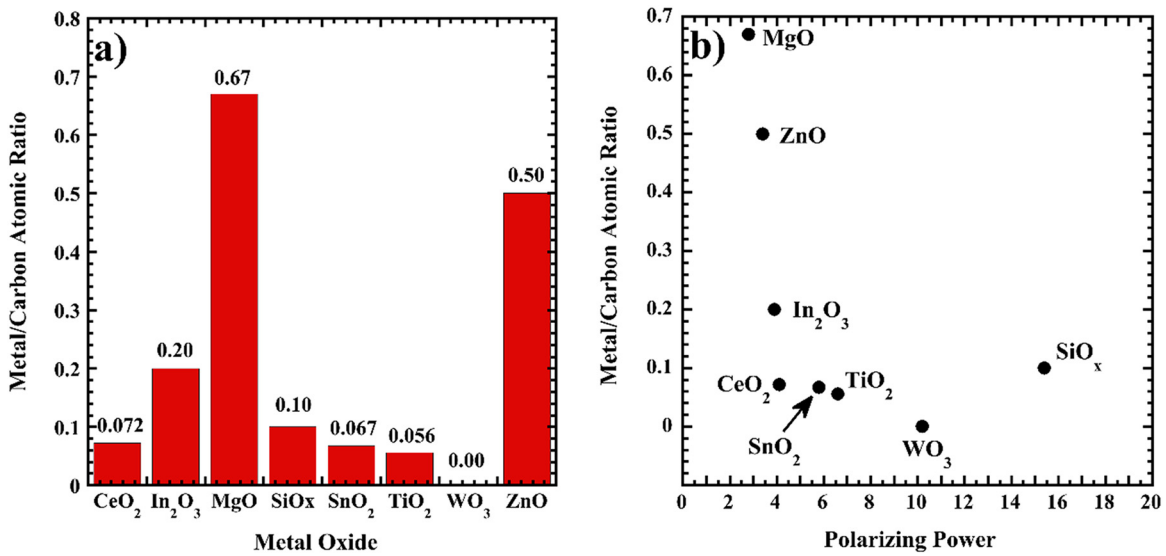

Fig. 8 a) Metal-to-carbon atomic ratios, determined from XPS, for the various MONPs deposited on plasma-treated PP (3 passes). b) Metal-to-carbon atomic ratio *versus* polarizing power of the MONPs.

Lewis acidity is that surface metal cations and oxide anions have incomplete coordination compared to their bulk counterparts and may act as Lewis acids and bases. Higher positive charge on the metal cation, and a smaller ionic radius, allow it to interact more strongly with environmental water and form adsorbed hydroxyl groups. Using recent data,[40] polarizing powers are calculated for the MONPs and included in Table 1. Fig. 8b displays a graph of the XPS metal-to-carbon atomic ratio *vs.* polarizing power. The dramatic inverse correlation between MONP surface concentration and polarizing power indicates that MONPs that are weak Lewis acids adhere significantly better than do strong Lewis acids. It should be noted that silica is a covalent metal oxide,[27,28] and polarizing power of its cation is not particularly meaningful, which may explain its deviation from the trend.

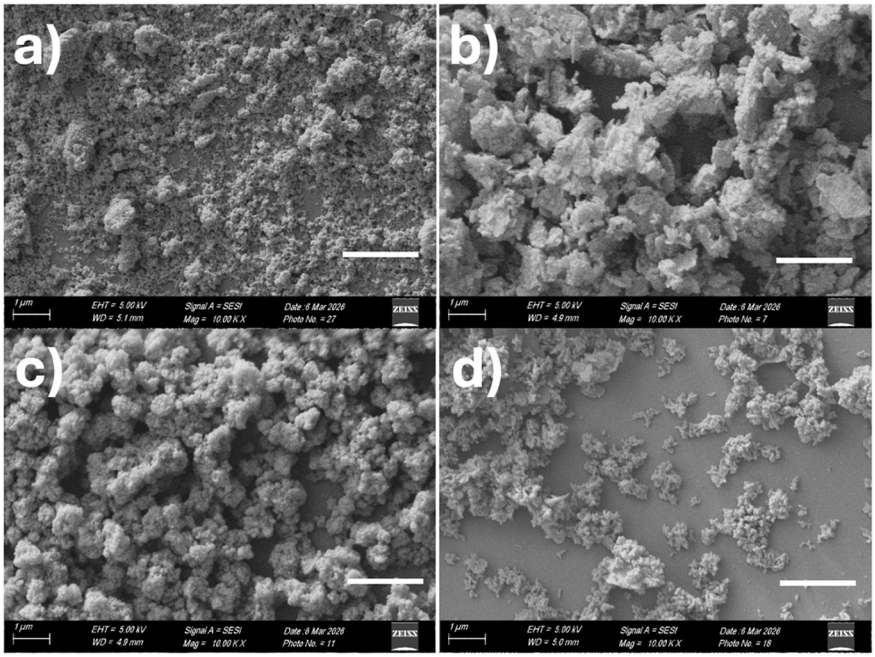

Fig. 9 FE-SEM images of a) CeO_2, b) MgO, c) TiO_2 and d) ZnO nanoparticles spray-coated onto glass slides to assess agglomeration behavior. The white scale bar in each image corresponds to 2 microns.

The greater adhesion of weak Lewis acid MONPs is most easily explained by realizing that the MONPs are hydroxylated. Therefore, the key interaction is between the hydroxyl groups of the MONPs and the carbonyl groups (and hydroxyl groups) of plasma treated PP. Strong Lewis acid MONPs will have less electron density on the oxygen atoms of their hydroxyl groups compared to weak Lewis acid MONPs. Therefore, hydroxyl groups adsorbed on strong Lewis acid MONPs will be less polar, and hydrogen bonding between the hydroxyl groups and the oxygen atoms of the carbonyl groups of PP will be weaker. Fig. 10 illustrates the concept using a terminal hydroxyl group on a generic metal cation and a carbonyl group on a PP surface. Of course, the actual situation is more complicated, with bridging hydroxyl groups also on the MONPs and other functional groups on the polymer surface. However, similar arguments could be made for those situations. It is noted that if there were not hydroxyl groups on the metal oxides, then other interactions would be at-play, such as direct interaction of the carbonyl groups on the PP surface with the metal cation. However, this type of interaction is largely disabled because of the presence of hydroxyl groups on the MONPs.

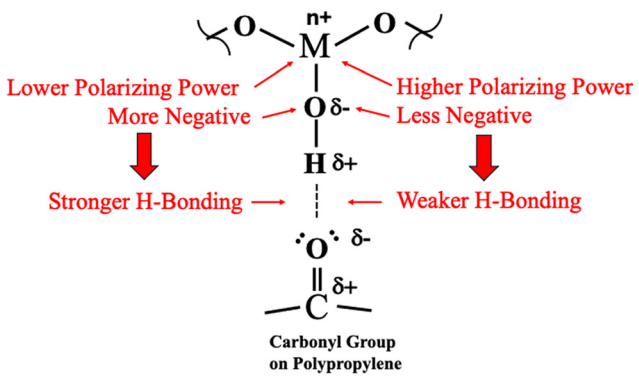

Fig. 10 Illustration of how the Lewis acidity of a metal oxide and the polarizing power of its cation could affect the hydrogen bonding of hydroxylated MONPs to plasma-treated PP.

It should further be noted that the situation in Fig. 10 is idealized. In reality, the MONP surfaces may contain other functional groups due to contaminating adsorbates (*e.g.*, carbonates from adsorbed carbon dioxide), and the surface density of adsorbed hydroxyl groups will depend on the MONP surface area and morphology. We also note that because the MONPs were dispersed in ethanol and spray-coated from their dispersions, ethanol will also be present on the MONPs and polypropylene fabric during the spray-coating process. It likely would form an intermediate layer between the hydroxyl groups of the MONPs and the carbonyl groups of the plasma-treated polymer until it evaporates. The details are unclear, but once evaporation has occurred, the situation depicted in Fig. 10 would apply. The use of water for dispersion would simplify the picture, but the MONPs do not disperse well in it.

Application to photocatalysis

Methyl paraoxon is a metabolic product of the pesticide methyl parathion; it also is an organophosphate nerve agent simulant. Its photocatalytic degradation in aqueous samples is, therefore, of some practical relevance. Fig. 11 shows UV-vis absorbance spectra of 8.0×10^{-5} M methyl paraoxon samples for different irradiation times with 365 nm light. As described earlier, one

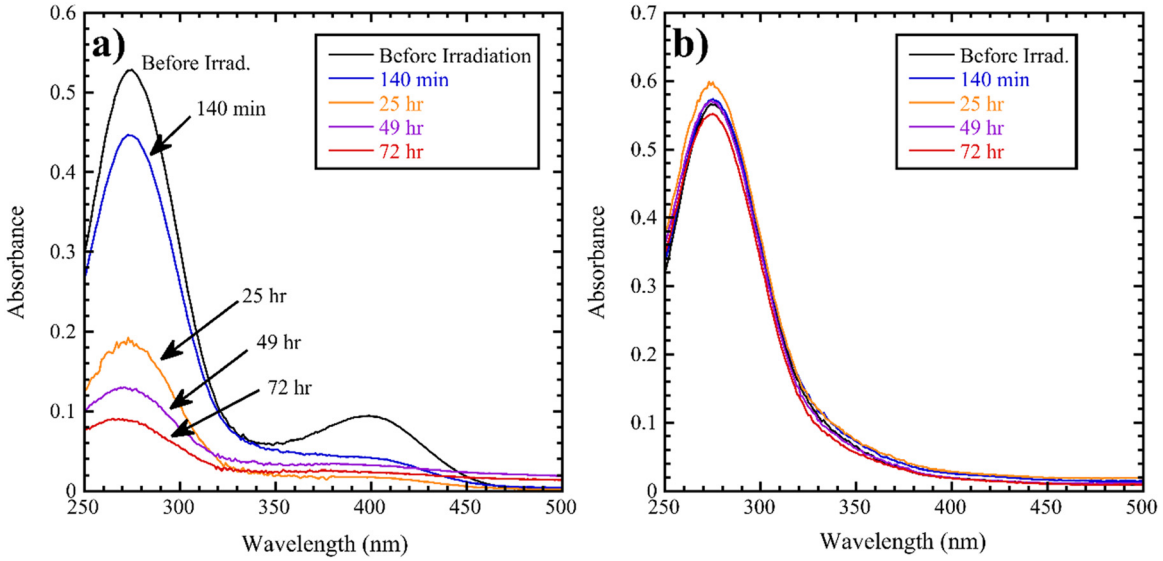

Fig. 11 UV-vis absorbance spectra of aqueous 8.0×10^{-5} M methyl paraoxon for various 365 nm irradiation times in the presence of a ZnO-functionalized PP swatch (a) and an unfunctionalized PP swatch (b). In both cases, 0.034 g of swatch material was used. The peak at 400 nm is due to a small amount of nitrophenol present prior to photocatalytic degradation.

cuvette contained a swatch of ZnO-functionalized PP, and the other contained an unfunctionalized PP swatch; both PP swatches had a mass of 0.034 g. Assuming that 2.9% of the functionalized swatch mass was due to ZnO NPs (see Table 1), the mass of ZnO on the swatch was *ca.* 1 mg.

Intact methyl paraoxon has peak absorbance at *ca.* 275 nm. As seen in the figure, a smaller peak is also present at *ca.* 400 nm prior to irradiation. This secondary peak is due to *p*-nitrophenol, indicating that there is some decomposition product present in this particular batch of methyl paraoxon. Fig. 11a shows that UV irradiation in the presence of the ZnO/PP leads to decomposition of both methyl paraoxon and *p*-nitrophenol, with the 275 nm absorbance peak decreasing from 0.53 to 0.09 after 72 h of irradiation. In contrast, Fig. 11b shows spectra from the control PP sample. It should be noted that the unirradiated control spectrum does not show the 400 nm absorbance peak due to *p*-nitrophenol, which is known to be pH sensitive. The presence of the ZnO on the PP swatch increases the pH enough for it to shift from being buried in the main 275 nm peak to absorbing at *ca.* 400 nm, as confirmed by experiments in which some base is added to the methyl paraoxon solution. These results demonstrate the use of open-air plasma treatment followed by spray-coating to immobilize photocatalytic nanoparticles onto polymer substrates.

Conclusions

A high throughput method of attaching MONPs to PP knitted fabric has been demonstrated. MONPs of similar size do not adhere equally well to open-air plasma-treated PP, with weak Lewis acid MONPs (such as MgO and ZnO) adhering better than strong Lewis acids (such as TiO_2 and WO_3). It has been shown that adhesion is inversely related to polarizing power of the metal oxide, which is a measure of its Lewis acidity. It is postulated that hydrogen bonding between the hydroxyl groups on the MONPs and plasma-induced moieties on PP, such as carbonyl groups, are responsible for the adhesion.

The method could be useful for various applications, including lithium ion battery separators and photocatalytic supports. In the latter application, it is important that MONPs remain attached, with high exposed surface area, as they are irradiated by light and decompose toxic liquids or gases. The use of open-air plasma treatment to fabricate ZnO-decorated PP fabric and its use for the photocatalytic decomposition of an organophosphorus pesticide, methyl paraoxon, has been demonstrated.

Open-air plasma treatment and spray-coating, routinely used for industrial applications, could be sequentially combined, followed by passing the treated fabric through an ultrasonicated bath and drying zone in a roll-to-roll process, to commercially produce MONP-coated PP surfaces and fabrics. The results of the present study indicate that the method is more useful for MONPs such as ZnO, for example, compared to TiO_2. Future work should investigate methods to improve the adhesion of strong Lewis acids such as TiO_2, since it is generally one of the most efficient of the simple photocatalytic metal oxides.

Conflicts of interest

There are no conflicts to declare.

Data availability

XPS data, ATR data, and UV-vis absorbance data for the photocatalysis measurements have been placed in a Mendeley data repository folder entitled "Data for Metal Oxide Adhesion

on PP". The data files are embargoed for 90 days until the paper is published. https://data.mendeley.com/datasets/v638hz53tr/1

Acknowledgements

This work was supported by the U.S. Army Combat Capabilities Development Command Soldier Center under grant W911QY-20-2-0005, through the HEROES initiative at UMass Lowell. We thank Dr. Gregory Peterson and Dr. Natalie Pomerantz for helpful discussions. This manuscript has been approved for public release: PR2025-2940.

References

1 Z. Dai, J. Zhu, J. Yan, J. Su, Y. Gao, X. Zhang, Q. Ke and G. N. Parsons, An advanced dual-function MnO_2-fabric air filter combining catalytic oxidation of formaldehyde and high-efficiency fine particulate matter removal, *Adv. Funct. Mater.*, 2020, **30**, 2001488.

2 A.-K. Mueller, Z.-K. Xu and A. Greiner, Sustainable electrospun affinity membranes for water remediation by removing metal and metal oxide nanoparticles, *ACS Appl. Polym. Mater.*, 2021, **3**, 5739–5748.

3 N. L. Pomerantz, E. E. Anderson, N. P. Dugan, N. F. Hoffman, H. F. Barton, D. T. Lee, C. J. Oldham, G. W. Peterson and G. N. Parsons, Air, water vapor, and aerosol transport through textiles with surface functional coatings of metal oxides and metal-organic frameworks, *ACS Appl. Mater. Interfaces*, 2019, **11**, 24683–24690.

4 I. Fatimah, G. Fadillah, I. Yanti and R. Doong, Clay-supported metal oxide nanoparticles in catalytic advanced oxidation processes: A review, *Nanomater.*, 2022, **12**, 825.

5 K. Li, Y. de Rancourt, X. de Mimerand, J. Jin and J. Guo Yi, Metal oxide (ZnO and TiO_2) and Fe-based metal-organic framework nanoparticles on 3D-printed fractal polymer surfaces for photocatalytic degradation of organic pollutants, *ACS Appl. Nano Mater.*, 2020, **3**, 2830–2845.

6 S. Li, G. He and J. Huang, Self-assembly on natural cellulose: Towards high-efficient catalysts, *Curr. Opin. Colloid Interface Sci.*, 2023, **63**, 101655.

7 B. Bai, L. Qiu, D. Mei, Z. Jin and L. Song, P, Du, Firmly-supported porous fabric fiber photocatalysts: TiO_2/porous carbon fiber cloth composites and their photocatalytic activity, *Mater. Res. Bull.*, 2022, **148**, 111672.

8 B. Baruah, L. Downer and D. Agyeman, Fabric-based composite materials containing ZnO-NRs and ZnO-NRs-AuNPs and their application in photocatalysis, *Mater. Chem. Phys.*, 2019, **231**, 252–259.

9 D. Markovic, Z. Saponjic, M. Radoicic, T. Radetic, V. Vodnik, B. Potkonjak and M. Radetic, Sonophotocatalytic degradation of dye C.I. acid orange 7 by TiO_2 and Ag nanoparticles immobilized on corona pretreated polypropylene non-woven fabric, *Ultrason. Sonochem.*, 2015, **24**, 221–229.

10 M. M. Rashid, B. Simoncic and B. Tomsic, Recent advances in TiO_2-functionalized textile surfaces, *Surf. Interfaces*, 2021, **22**, 100890.

11 D. Wood, S. Shaw, T. Cawte, E. Shanen and B. Van Heyst, An overview of photocatalyst immobilization methods for air pollution remediation, *Chem. Eng. J.*, 2020, **391**, 123490.

12 H. M. Ouyang, H. Y. Xu, G. T. Fei, S. H. Xu, X. F. Li, W. C. Chen and S. J. Li, Binder-free SiO_2 nanoparticles coated polypropylene separator for high performance lithium-ion battery, *Solid State Ionics*, 2025, **420**, 116783.

13 M. Chen, Y. Fan, H. Zhou and G. Li, ZnO@C coated cellulose-based separators control lithium deposition direction to stable lithium metal batteries, *Small*, 2024, **20**, 2306712.

14 K. Thinkohkaew, T. Piroonpan, N. Jiraborvornpongsa and P. Potiyaraj, Development of multifunctional polypropylene nonwoven fabric by radiation induced grafting of TiO_2 nanoparticles and trifluoroethyl methacrylate for protective textile applications, *Materialia*, 2022, **21**, 101355.

15 M. Shaban, F. Mohamed and S. Abdallah, Production and characterization of superhydrophobic and antibacterial coated fabrics utilizing ZnO nanocatalyst, *Sci. Rep.*, 2018, **8**, 3925.

16 D. T. Lee, J. Zhao, C. J. Oldham, G. W. Peterson and G. N. Parsons, UIO-66-NH_2 metal-organic framework (MOF) nucleation on TiO_2, ZnO, and Al_2O_3 atomic layer deposition-treated polymer fibers: Role of metal oxide on MOF growth and catalytic hydrolysis of chemical warfare agent simulants, *ACS Appl. Mater. Interfaces*, 2017, **9**, 44847–44855.

17 W. J. Sweet III, J. S. Jur and G. N. Parsons, Bi-layer Al_2O_3/ZnO atomic layer deposition for controllable conductive coatings on polypropylene nonwoven fiber mats, *J. Appl. Phys.*, 2013, **113**, 194303.

18 K. Turlakiewicz, S. Sztajnowski, W. Sujka, I. Krucinska, G. Szparaga and M. Puchalski, Investigation of PP monofilament structural changes with various conditions used for deposition of TiO_2 atomic layers by ALD technique, *Polym. Test.*, 2023, **124**, 108065.

19 G. Gurbandurdyyev, M. Kissan, L.-V. Delumeau, J. Y. Loke, C. H. Teoh, J. Cheon, F. Ye, K. C. Tam and K. P. Musselman, Robust, conformal ZnO coatings on fabrics via atmospheric-pressure spatial atomic layer deposition with in-situ thickness control, *ChemNanoMat*, 2023, **9**, e202200498.

20 X. Qian, S. Xiong, Y. Rao, Z.-X. Low, Z. Zhong and Y. Wang, Atomic layer deposition of ZnO on polypropylene nonwovens for photocatalytic antibacterial facemasks, *NANO*, 2023, **34**, 255701.

21 Y. de Rancourt, B. Couturaud, A. Mas and J. J. Robin, Synthesis of antibacterial surfaces by plasma grafting of zinc oxide based nanocomposites onto polypropylene, *J. Colloid Interface Sci.*, 2013, **402**, 320–326.

22 I. Unlu, J. W. Soares, D. M. Steeves, R. Pang, E. A. Welsh and J. E. Whitten, Multifunctional metal oxide nanoparticle decorated polypropylene knitted swatches, *J. Mater. Sci.*, 2018, **53**, 1514–1526.

23 J.-P. Booth, M. Mozetic, A. Nikiforov and C. Oehr, Foundations of plasma surface functionalization of polymers for industrial and biological applications, *Plasma Sources Sci. Technol.*, 2022, **31**, 103001.

24 C. Ruzafa-Silvestre, V. M. Serrano-Martinez, F. Aran-Ais and E. Orgiles-Calpena, Durability of the effectiveness of atmospheric plasma treatment applied to thermoplastic styrene-butadiene-styrene (SBS) rubber, *J. Adhes.*, 2025, **101**, 164–190.
25 H. T. Sasmazel, M. Alazzawi and N. K. A. Alsahib, Atmospheric pressure plasma surface treatment of polymers and influence on cell cultivation, *Molecules*, 2021, **26**, 1665.
26 Y. J. Tak, F. Hilt, S. Keene, W.-G. Kim, R. H. Dauskardt, A. Salleo and H. J. Kim, High throughput open-air plasma activation of metal-oxide thin films with low thermal budget, *ACS Appl. Mater. Interfaces*, 2018, **10**, 37223–37232.
27 G. Busca, The surface acidity and basicity of solid oxides and zeolites, in *Metal Oxides: Chemistry and Applications*, CRC Taylor & Francis, Boca Raton, FL, 2006, pp. 247–318.
28 G. Busca, Bases and basic materials in chemical and environmental processes, Liquid versus solid basicity, *Chem. Rev.*, 2020, **110**, 2217–2249.
29 D. Briggs, *Surface Analysis of Polymers by XPS and Static SIMS*, Cambridge University Press, Cambridge, U.K., 1997.
30 C. D. Wagner, W. M. Riggs, L. E. Davis, J. F. Moulder and G. E. Muilenberg, *Handbook of X-Ray Photoelectron Spectroscopy*, Perkin-Elmer Corp, Eden Prairie, MN, 1979.
31 K. G. Kostov, T. M. C. Nishime, L. R. O. Hein and A. Toth, Study of polypropylene surface modification by air dielectric barrier discharge operated at two different frequencies, *Surf. Coat. Technol.*, 2013, **234**, 60–66.
32 R. Morent, N. De Geyter, C. Leys, L. Gengembre and E. Payen, Comparison between XPS- and FTIR-analysis of plasma-treated polypropylene film surfaces, *Surf. Interface Anal.*, 2008, **40**, 597–600.
33 G. Socrates, *Infrared and Raman Characteristic Group Frequencies: Tables and Charts*, 3rd. ed., Wiley, Chichester, U. K., 2004.
34 J. Fang, L. Zhang, D. Sutton, X. Wang and T. Lin, Needleless melt-electrospinning of polypropylene nanofibres, *J. Nanomater.*, 2012, **2012**, 1–9.
35 M. H. Wu, C. C. Wang and C. Y. Chen, Preparation of high melt strength of polypropylene by addition of an ionically modified polypropylene, *Polymer*, 2020, **202**, 122743.
36 J. Singh, A. Mukherjee, S. K. Sengupta, J. Im, G. W. Peterson and J. E. Whitten, Sulfur dioxide and nitrogen dioxide adsorption on zinc oxide and zirconium hydroxide nanoparticles and the effect on photoluminescence, *Appl. Surf. Sci.*, 2012, **258**, 5778–5785.
37 S. Kim, R. M. D. S. Somaratne and J. E. Whitten, Effect of adsorption on the photoluminescence of zinc oxide nanoparticles, *J. Phys. Chem. C*, 2018, **122**, 18982–18994.
38 M. T. Norma, N. Amor and M. Petru, Synthesis and applications of ZnO nanostructures (ZONSs) and a review, *Crit. Rev. Solid State Mater. Sci.*, 2022, **47**, 99–141.
39 Y. Xia, J. Wang, R. Chen, D. Zhou and L. Xiang, A review on the fabrication of hierarchical ZnO nanostructures for photocatalysis application, *Crystals*, 2016, **6**, 148.
40 F. C. Hawthorne and O. C. Gagne, New ion radii for oxides, oxysalts, fluorides, chlorides, and nitrides, *Acta Crystallogr., Sect. B:Struct. Sci., Cryst. Eng. Mater.*, 2024, **80**, 326–339.